Optoelectronic and structural characterization of trapezoidal defects in 4H-SiC epilayers and the effect on MOSFET reliability

View Online   Export Citation   CrossMark

Sami A. El Hageali,[1,2,a] Harvey Guthrey,[2] Steven Johnston,[2] Andrew Norman,[2] Jake Soto,[3] Bruce Odekirk,[3] Robert E. Stahlbush,[4] Nadeemullah A. Mahadik,[4] Brian P. Gorman,[1] and Mowafak Al-Jassim[2]

AFFILIATIONS

[1]Colorado School of Mines, 1500 Illinois Street, Golden, Colorado 80401, USA
[2]National Renewable Energy Laboratory, 15013 Denver West Parkway, Golden, Colorado 80401, USA
[3]Microchip Technology Inc., 405 SW Columbia Street, Bend, Oregon 97702, USA
[4]Naval Research Laboratory, 4555 Overlook Ave SW, Washington, DC 20375, USA

[a]Author to whom correspondence should be addressed: elhageali@mines.edu

ABSTRACT

To this day, trapezoidal defects are found in clusters and high counts in wafers representing the industry standard in terms of material quality being produced. This study sheds light on the nature, origin, behavior, and impact of this defect on device yield and reliability. Trapezoidal defects in 4H-SiC epitaxial layers were investigated by photoluminescence (PL) imaging, scanning electron microscopy (SEM), cathodoluminescence spectrum imaging (CLSI), SEM electron beam induced current (EBIC) imaging, and by transmission electron microscopy (TEM) observation. The bar-shaped stacking faults were identified by the PL and CL measurements with a peak emission wavelength of 420 and 450 nm. An optoelectronic behavioral study based on the recombination enhanced dislocation glide mechanism revealed how expanding dislocations and stacking faults interact with each other. Combining the luminescence and microscopy results, the nature of the stacking faults was identified as being a combination of Shockley-type and Frank-type stacking faults. The TEM analysis showed that these defects originate from the substrate and the stacking sequences of some of the faults were determined as (…2, 4, 2…) and (…2, 3, 2…) in the Zhdanov's notation by high-resolution TEM. The origin of this defect is speculated based on our results and previous reports. The EBIC imaging showed that the high density of SFs in these towers is a strong site of carrier recombination, which presumably has an impact on the transfer characteristics of SiC devices. Furthermore, these defects have shown to impact metal oxide semiconductor field effect transistors electrical performance via an increase in the on-state resistance depending on the coverage percentage of the tower of defects in the active area of the device.

I. INTRODUCTION

Silicon carbide (SiC) metal oxide semiconductor field effect transistors (MOSFETs) are rapidly displacing silicon (Si) insulated-gate bipolar transistors (IGBTs) and other types of bipolar transistors for high power applications. This is due to its 3× higher breakdown field, lower on-state resistance, higher breakdown voltage, and high thermal conductivity, which leads to lower switching losses and higher efficiency. The 4H-SiC polytype has the highest bandgap and is generally preferred to other SiC polytypes in practical power device manufacturing. SiC devices, such as Schottky diodes and FET/MOSFETs, are being used in converters, inverters, power supplies, battery chargers, and motor control systems for 5G infrastructures, electric vehicles (EVs), renewable energy generation, and data centers. Even though single-crystal 4H-SiC wafers of 200 mm diameter are now being commercialized, a variety of issues make SiC devices difficult to fabricate with high yield and reliability.

TABLE I. Characteristic luminescence emissions of extended defects in 4H-SiC epilayers.

Defects	Nature	Characteristic luminescence emissions
TSD[14–16]	$\mathbf{b} = \langle 0001 \rangle$	600–950 nm and peaking at 800 nm at RT
		700–950 nm at 78 K
TED[14–16]	$\mathbf{b} = 1/3 \langle 11 - 20 \rangle$	> 700 nm and peaking at > 900 nm at RT > 850 nm at 78 K
BPD[2,16–19]	b = Screw or edge or mixed	
	C-core	720–850 nm and 920–930 nm
	Si-core	650–870 nm at RT
Single Shockley fault[20]	(3,1)	420 nm at RT
Double Shockley fault[20,21]	(6,0)	500 nm at RT
Triple Shockley fault[20,22]	(3,5)	480 nm at RT
8H fault[23,24]	(4,4)	455 nm at RT
		467 nm ~100 K
		(463, 668, 472, 473 nm) ~9 K
		(471, 477, 480, 482 nm) ~5 K
Multilayer Frank fault[25]	(4,2) but can be different depending on the number of conversions to reach the original sequence	457 nm at RT
		(450, 455, 458, 460 nm) at T < 10 K
Extrinsic Frank fault[25]	(4,1)	424 nm at RT
		(415, 419, 423, 425 nm) at T < 10K
Intrinsic Frank fault[25]	(5,2)	488 nm at RT
		(478, 485, 488, 490 nm) at T < 10 K
Near band-edge	(2,2)	390 nm at RT

The progress in SiC device development relies on low defect substrate and epitaxial growth technology. Indeed, material defects in SiC are the root cause of many technological challenges faced by SiC manufacturers. Defects such as stacking faults (SFs), basal plane dislocations (BPDs), and threading dislocations (TDs) found in SiC epilayers and substrates can affect the performance and reliability of SiC devices. Over the past two decades, a wide range of stacking faults have been identified using various luminescence techniques (cathodoluminescence, photoluminescence, electroluminescence) coupled with microscopy techniques such as electron beam induced current (EBIC) and TEM. The origin and impact of such stacking faults and dislocations on electrical device performance have been reported by several groups in recent years. As examples, they can be responsible for an increase in the forward voltage drop and on-state resistance especially in bipolar devices, and an increase in reverse leakage current for all devices. For the rest of this study, Table I summarizes the most common stacking faults identified with their characteristic luminescence emission wavelengths and corresponding stacking sequences using the Zhdanov's notation. Dislocation behavior in SiC epitaxial layers has also been extensively studied. For example, it was found that most basal plane dislocations (BPDs) in SiC substrates are converted to threading edge dislocations (TEDs) during epitaxial growth.[1] Also, that the stacking faults are bounded by more energetically favorable partial dislocations, and that Si-core partials glide under device operation while C-core partials remain unmoved. The mechanism by which such dislocations glide occurs is well known in the field as the "recombination enhanced dislocation glide" (REDG) mechanism[2–6] and can cause stacking faults to expand significantly during prolonged device operation, which then results in the electrical degradation of SiC devices.

Currently, the density of most of these BPDs has been reduced through process controls as state-of-the-art grown epitaxial layers under $30\,\mu\text{m}$ thickness show an average of less than 1 BPD/150 mm wafer.[7] While such epitaxial layers are suitable for under 3.3 kV devices, the next generation of SiC 6.5–20 kV devices are also being developed. This generation requires the fabrication of thicker SiC epilayers. While defects that originate from the substrate and propagate into $30\,\mu\text{m}$ epilayers are not too critically averse to device performance due to their projected length, the results will be much more significant for thicker epilayers. SiC has still a substantially higher price than silicon, mainly due to the substrate manufacturing process and to its higher defect density, which reduces yield. Decreasing the defect density in both the substrate and epitaxial layer is critical to commercialize thick epilayers for 6.5+ kV devices. One defect found in the substrate that has been reported in the past is known as the "trapezoidal defect."[8–10] Trapezoidal defects, also called "bar-shaped stacking faults," are a major defect that are generated during bulk crystal growth on the basal plane. They propagate into the epitaxial layer and can span over several millimeters in the wafer.[8,9,11–13] This defect is still widespread in today's substrates and epitaxial layers, and continues to affect device performance in the long term. Unlike inclusions (also known as downfalls), BPDs and micropipes, trapezoidal defects are not considered as killer defects (causing failure during electrical screening tests) in the industry. Hence, trapezoidal defects can be present within a device while passing all electrical specifications. However, the long term degradation due to trapezoidal defects during extended operations is not yet fully understood and an extensive study detailing their nature, origin, and behavior under device operation and influence on devices is needed to understand their effect on long term reliability.

In this study, trapezoidal defects in 4H-SiC epitaxial layers were investigated by photoluminescence (PL) imaging, scanning electron microscopy (SEM), cathodoluminescence (CL) spectrum imaging, SEM electron beam induced current (EBIC) imaging, transmission electron microscopy (TEM) observation, and electrical measurements. The nature of the stacking faults present in these towers of defects is discussed using the UV-PL and CLSI results. In order to investigate their behavior under device operation, sequential UV-PL imaging with UV exposures was performed to analyze the motion and interaction of expanding dislocations/SFs via the REDG mechanism. EBIC imaging was used to understand the excess carrier recombination behavior at different defect sites. The TEM analysis was done to show the origin of trapezoidal defects and the stacking sequences of the faults are determined by high-resolution TEM (HR-TEM). Moreover, electrical measurements were performed on a 150 mm diameter commercial 4H-SiC wafer with MOSFETs having this type of defect. The complete understanding of this defect provided in this paper is necessary to develop mitigation strategies against its prevalence and achieve the quality that the next generation of 6.5+ kV SiC devices requires.

II. EXPERIMENTAL

In a lot of 12 wafers commercially obtained, few of the wafers showed the presence of this defect. In order to perform this study, one wafer having clusters of trapezoidal defects in multiple locations were pulled out for destructive analysis. Since this defect is identical across defect wafers, the selected wafer is representative of others. Hence, the destructive analysis does not need to be performed on multiple wafers. One other wafer was sent on through the line for MOSFET fabrication in order to study the impact of this defect on yield. The wafers purchased in this study are all designed for a 3.3 kV rating and therefore all have the same doping concentrations and thicknesses in the respective layers across the wafers. Hence, the wafers used in this study are all comparable.

The specimen used in this study for destructive analysis is from commercial 4H-SiC state-of-art wafers with a $30 \, \mu m$-thick epitaxial layer lightly n-type doped ($Nd = 3 \times 10^{15} \, cm^{-3}$) and a $3 \, \mu m$-thick buffer layer ($Nd = 3 \times 10^{18} \, cm^{-3}$). The epitaxial layer was commercially grown on 4° off the c axis 4H-SiC n-type conductive substrate ($Nd = 3 \times 10^{18} \, cm^{-3}$) using chemical vapor deposition (CVD).

For ultraviolet-PL (UV-PL) imaging, the images were collected while the sample was housed in a dark enclosure at room temperature using a Princeton Instruments PIXIS 1024BR Si-charge-coupled device (CCD) with a top view setup. The camera was cooled to −60 °C to reduce background counts, and the total background and read-out noise was only about 1% of the 16-bit pixel capacity; thus, no background image was needed for subtraction. The UV excitation line used in this study was from a 360 nm laser diode which has a $50 \, \mu m$ penetration depth.[26] The excited volume was a 1-mm laser spot size across the thickness of the epilayer. For an accurate identification of the nature of stacking faults, an automated filter wheel from Edmund Optics with six positions was used to change the output filters for each acquisition. Each PL image was filtered by a narrow (Full width at half maximum <10 nm) bandpass filter at 420, 450, 480, 488, 500, and 550 nm. A long-pass (LP) filter (LP > 700 nm) was

used to observe BPD partials, which allowed us to see the entire structure of the defect. Image acquisition times can range from seconds to minutes, and for this sample in particular, exposure times of 3 min and 30 s were adequate to collect the PL images at high and low resolution, respectively, and nearly fill the detector pixels. The uncropped images have a resolution of 1024×1024 pixels. For the high spatial resolution PL images, we used a Mitutoyo 20× microscope objective with 0.40 numerical aperture and 20 mm working distance coupled with a Navitar Zoom 6000 lens. The images acquired with this lens system have a field of view (FOV) of $\sim 1.3 \times 1.3 \, mm^2$. For the lower resolution PL images, a Unifoc-12 Schneider macro-imaging lens was used, which provides a FOV of $\sim 4 \times 4 \, mm^2$. In general, when using bandpass filters, bright regions [Fig. 1] correspond to strong
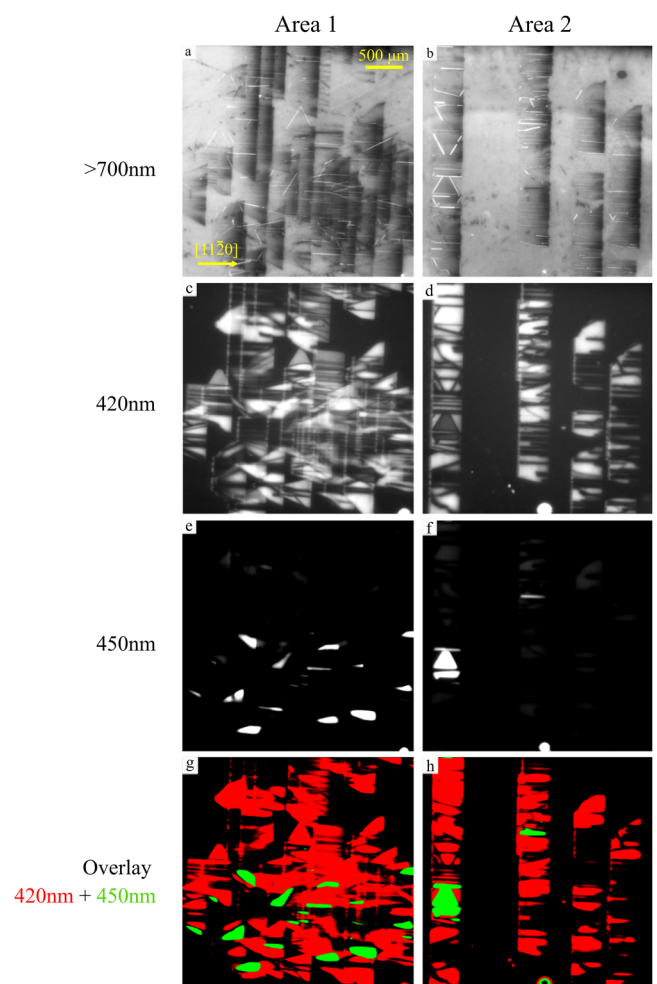
FIG. 1. UV-PL images of trapezoidal defects in two areas, area 1 and area 2, collected with different bandpass filters: (a, b) LP > 700 nm, (c, d) bandpass 420 nm, (e, f) bandpass 450 nm with a FWHM < 10 nm, and (g, h) overlay composite images of (c, e) and (d, f), respectively. The scale is the same for all images.

luminescence within the corresponding wavelength range, whereas dark regions indicate the opposite (i.e., no characteristic luminescence in that range). For the *in situ* UV-PL movies, the beam was scanning over the defect area for the whole duration of the image sequence using optical frequency mirrors. The stack of images was then processed, and the image stack was created. It is to be noted that the luminescence observed in the UV-PL images is from the epilayer and the buffer layer.

CL spectrum imaging was performed in a JEOL 7600F field-emission SEM with a Horiba H-CLUE CL system. Samples were cryogenically cooled in the SEM on a Gatan CF302 continuous-flow liquid-helium cold stage to a nominal temperature of 6 K. The SEM beam conditions were 15 kV accelerating voltage and about 3 nA beam current. The effective electron penetration depth in 4H SiC is $\sim$2 μm for accelerating voltage of 15 kV.[27] Spectrum-per-pixel data collection and global spectra acquisition was accomplished using a parabolic light-collection mirror and an iHR320 spectrometer equipped with a deep Silicon Syncerity thermoelectrically cooled CCD detector (1024 × 256 pixels) system. Data were then processed to produce integrated intensity images, peak emission maps, and CL spectra from different regions of the samples.

Site-specific TEM lift-outs of defects were made via EBIC imaging in a dual beam focused Ga$^+$ ion beam (FIB) workstation (FEI Nova NanoLab 200 FIB/SEM). After identifying a region in EBIC (device: AuPd/SiC/Ag) and prior to milling, a $\sim$1 μm-thick layer of Pt (e-beam Pt + FIB Pt) was locally deposited on top of the region of interest to even out the top surface roughness and to protect the final analysis area from incident ions during TEM sample preparation. The TEM cross section specimen was then prepared by standard FIB lift-out methods. A 30-kV ion beam carved out the initial bevel shape and a 5 kV beam created the final beveled surface to reduce surface damage. Ga$^+$ ion FIB damage is further removed by low energy (<1 kV) Ar$^+$ ion milling while cooling the sample using liquid N$_2$ in a Fischione NanoMill. Diffraction and high-resolution TEM imaging were then performed on the prepared sample using two different TEMs, FEI Tecnai F20 UT operated at 200 kV and a FEI Tecnai ST30 TEM operated at 300 kV. The high-resolution TEM images were processed using Fourier filtering of the original images to better see the stacking sequences. The low-magnification diffraction contrast images are shown as acquired.

III. RESULTS AND DISCUSSION

Figure 1 depicts the UV-PL images in two different areas from an epitaxial layer, area 1 Figs. 1(a), 1(c), 1(e), 1(g) and area 2 Figs. 1(b), 1(d), 1(f), 1(h), containing trapezoidal defects acquired with different bandpass filters. UV-PL images in Figs. 1(a) and 1(b) are acquired using a long-pass >700 nm filter to show the inner structure of this tower of defects and reveal the dislocation network, common dislocation related emission is summarized in Table I. It is important to notice the tremendous amount of BPDs that constitute these towers. It is clear from the UV-PL images that most of these dislocations are partial dislocations delineating stacking faults. The trapezoidal defect towers were observed to vary in size from 500 μm to 4 mm in length perpendicular to the step flow

direction. According to the direction of the upstream growth step flow and calculation of their width, these defects propagate from the interface epi/substrate interface to the top surface at 4° off-cut angle on the basal plane. Figures 1(c)–1(f) show emission from two wavelength bands, 420 and 450 nm, which correspond to two types of SFs. Based on the range of wavelength emissions shown in Table I, SF1 in Figs. 1(c) and 1(d) emitting with the 420 nm bandpass filter most likely corresponds to an extrinsic Frank-type SF (EFSF) or a single Shockley SF (1SSF). This bar-shaped SF is very close in emission wavelength to the single Shockley (1SSF). However, the 1SSF is most commonly found to be triangular shaped and the bar-shaped SF has been discussed as being towers of EFSFs in previous reports.[8,9] According to Table I, SF2 in Figs. 1(e) and 1(f) is identified to correspond to a multilayer Frank-type SF or an 8H SF. Its nature will be discussed in a subsequent section. Figures 1(g) and 1(h) are overlay composite images from the corresponding 420 and 450 nm UV-PL acquisitions which make the distinction between the two characteristic wavelength emissions (420 and 450 nm) by applying correction factors to pixel intensity values such as camera QE efficiency percentage and intrinsic transmission properties of the filters. For the rest of this study, we will call SF1 the SFs emitting in the $\sim$420 nm range and SF2, the SFs giving out emission in the $\sim$450 nm range.

Interestingly, Fig. 2 shows that these towers of defects are made of stacking faults bounded by dislocations propagating along the step-growth [11–20] direction. A linear density can, therefore, be used to describe the concentration of dislocations in the towers by looking in a direction perpendicular to the [11–20] direction. Figures 2(c) and 2(d) are plots obtained from line profile AB and CD in Figs. 2(a) and 2(b), respectively. Line profile AB goes vertically through a region of trapezoidal defects having only [11–20] oriented dislocation lines (PD1-PD12). Through the AB intensity profile, the first striking observation is that PD12 is the brightest dislocation line and is three times brighter than PD1. PD2 is a bright partial dislocation that is spatially close to a fainter dislocation PD3. PD4 seems to have a similar intensity with PD2. PD5-PD11 all have luminescence intensities just above background. Along line profile AB and between PD1 and PD2, there are a bunch of dislocations that are not bright enough to be distinguished at this magnification and are shown in Figs. 2(b) and 2(d).

As it can be seen in Fig. 2(b) and along CD, dislocations PD1, PD4, PD6–8 have low PL emissions and are not easily visible in Fig. 2(a) due to magnification and weak luminescence signals. As the spectra in Fig. 2(d) suggests, these dislocations are almost as bright as background and are thus, difficult to observe. Along line profile CD, PD2 in Fig. 2(b) is a Si-core dislocation bounding a Shockley stacking fault and is bright. Indeed, this triangular shaped pattern is highly recognizable as morphology of Shockley-type SFs with Si-core partials lying in the Peierls valley direction which results in the splitting of a perfect BPD. This dislocation was already present and does not result from UV-exposure. The bright visible spots along the angled horizontal dislocation at PD3 are where these Si-core dislocations bounding the Shockley SFs originate from. It is important to note that these stacking faults already exists but are not visible due to magnification limit. Figures 2(a) and 2(b) suggest that these towers of defects might contain many more dislocations than expected. When observed at low
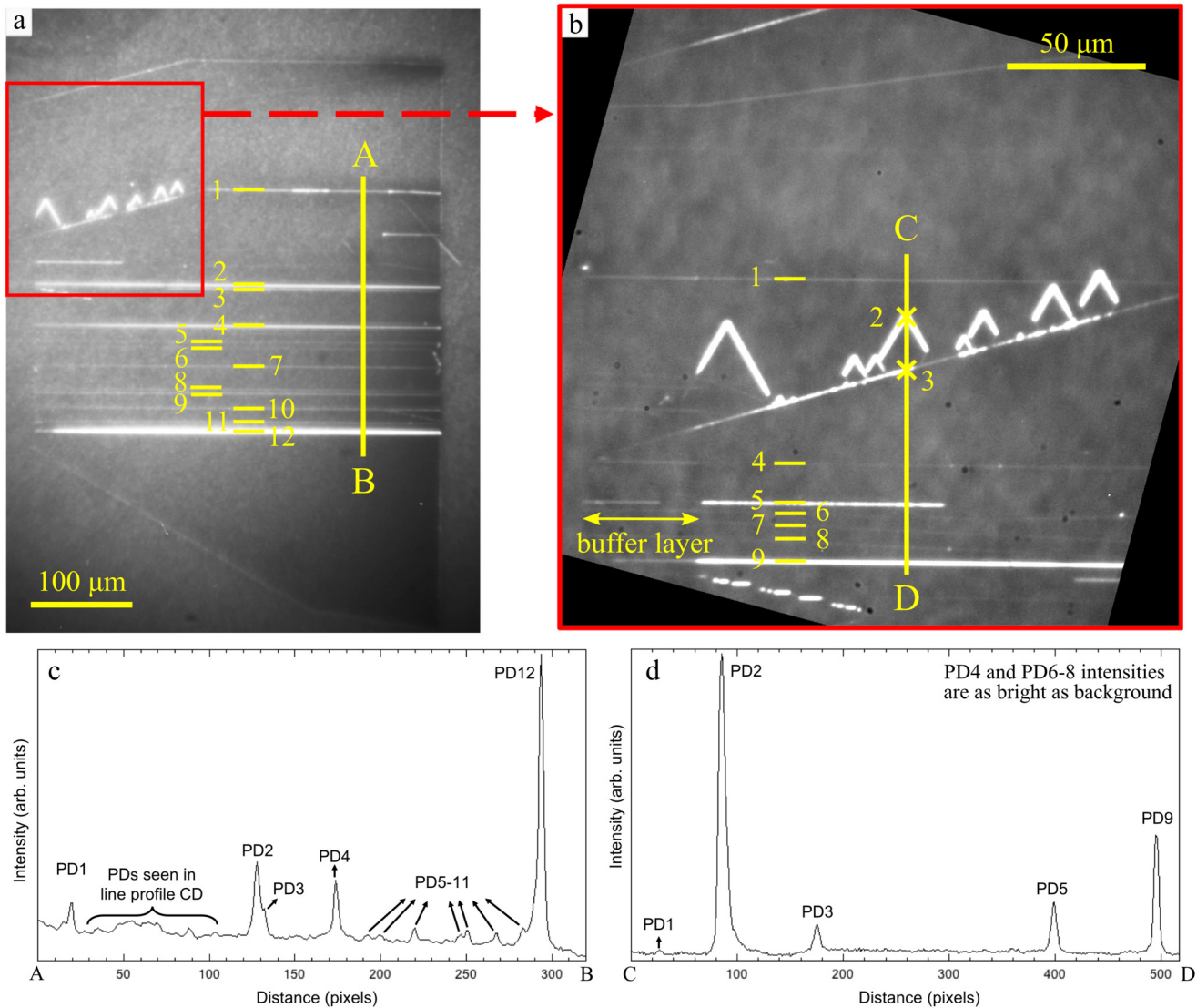
FIG. 2. UV-PL image of (a) a short trapezoidal defect acquired with a LP > 700 nm and, (b) UV-PL image acquired at higher magnification corresponding to the red box in (a). (c) and (d) are line plot profiles from line profiles AB and CD shown in (a) and (b), respectively, describing the luminescence intensity of dislocations in trapezoidal defects.

magnification (along AB), 12 BPDs are clearly visible and labeled. However, at higher magnification (along CD), four more dislocations show up. One should be careful when assessing the dislocation density in trapezoidal defect towers.

It is to note that the PL intensity at PD3, along CD, is low compared to PD5 and PD9. PD3 is located right along a fainter dislocation line so it could appear less bright due to its interaction with a Shockley partial. This could also explain the difference in intensity observed at PD5 and PD9 along CD. The recombination behavior at these locations is expected to be different than from a completely only pure bright dislocation, such as PD2 along CD, or completely pure faint dislocation, such as at PD1 along CD. Overall, line profiles AB and CD show that these dislocations yield significantly different luminescence intensities which means that they are potentially of different chemical nature. From this figure only, it is difficult to attribute the Si-core or C-core nature of the dislocations simply based on the PL intensity. This difference in intensity was previously reported by multiple groups.[2,16–19] It was reported that C-core dislocations are much less luminescent than Si-core dislocations and that they luminesce in different wavelength

11 September 2023 21:39:17

ranges (see Table I). Even if some dislocations are brighter than the others in Fig. 2, the analysis of PL intensity to understand dislocation core-type can be quite complex so the authors decide not to assign the core-type of the observed dislocations. The purpose of this figure is to show the variety of luminescence features from this defect, the density of dislocations, and explain that they can be made of dislocations of different nature. Also, PL intensity being one factor for the identification of the core-type, the second factor which is dislocation motion should be monitored to distinguish Si-core from C-core dislocations. For this reason, the nature of the dislocations is not discussed in Fig. 2. For our next experiment, in order to understand and simulate the behavior of such dislocations during device operation, we experimentally induce localized dislocation motion via high intensity *in situ* UV-PL imaging. This experiment relies on the REDG mechanism (expansion of dislocations) to understand the motion of C- and Si-core dislocations and their interactions. It is well known in the field that Si-core dislocations are glissile and C-core dislocations are sessile.[2,4,16,18,19,28–32] Indeed, multiple reports showed that the glide activation energy of Si-core dislocation is much lower that C-core dislocations. It is also speculated that C-core dislocations contain impurities and have a more stable core that prevent them from gliding. Thus, the following experiment also allows to confirm the nature of the partials. The *in situ* ultra-high intensity UV-PL has been done on specific locations at low magnification [Fig. 3, Multimedia available online] and high magnification [Fig. 5, Multimedia available online].

Figure 3 (Multimedia available online) shows the *in situ* evolution over time of the dislocations' glide. In Fig. 4 at time t1, it is shown that the Si-core partials are massively originating from C-core partial. Again, these dislocations are originally present really close to the C-core partial but cannot be observed due to resolution limits. These Si-core 30° partial dislocations bounding triangular SFs are characteristics of Shockley-type stacking faults as mentioned earlier. The non-motion of the fainter dislocation lines lying along the [11–20] direction can be explained in two possible ways. They can be of Frank-nature or are C-core dislocations. Let us discuss these two possibilities.

First, as reported by Camarda *et al.*,[9] the dislocations in bar shaped defects bound EFSFs and result from the combination of two Shockley-type and one Frank-type SF. Thus, these fainter dislocations should have Burgers vector component of screw and edge type with respect to the [11–20] dislocation line: an edge-type c axis component of the Burgers vector from Frank-type dislocations + a [11–20] Burgers vector screw component from the Shockley type. Second possibility, they are C-core-type dislocations which as mentioned above, do not glide. For certain, the Frank-type nature of these dislocations and the edge Burgers vector component render the dislocation sessile, and that is the reason why no motion is observed in Fig. 4 from t1-t12 from the fainter dislocations. Due to the combined nature of these dislocations, it is difficult to speculate on their core-nature. Assuming a C-core nature to justify the sessile configuration of this dislocation would be too speculative and therefore it is explained through its partial Frank-type nature.

On the other hand, the mobile Si-core dislocations glide via the REDG mechanism in response to a locally applied carrier injection in the crystal. From Fig. 4, it can be noted that the marked
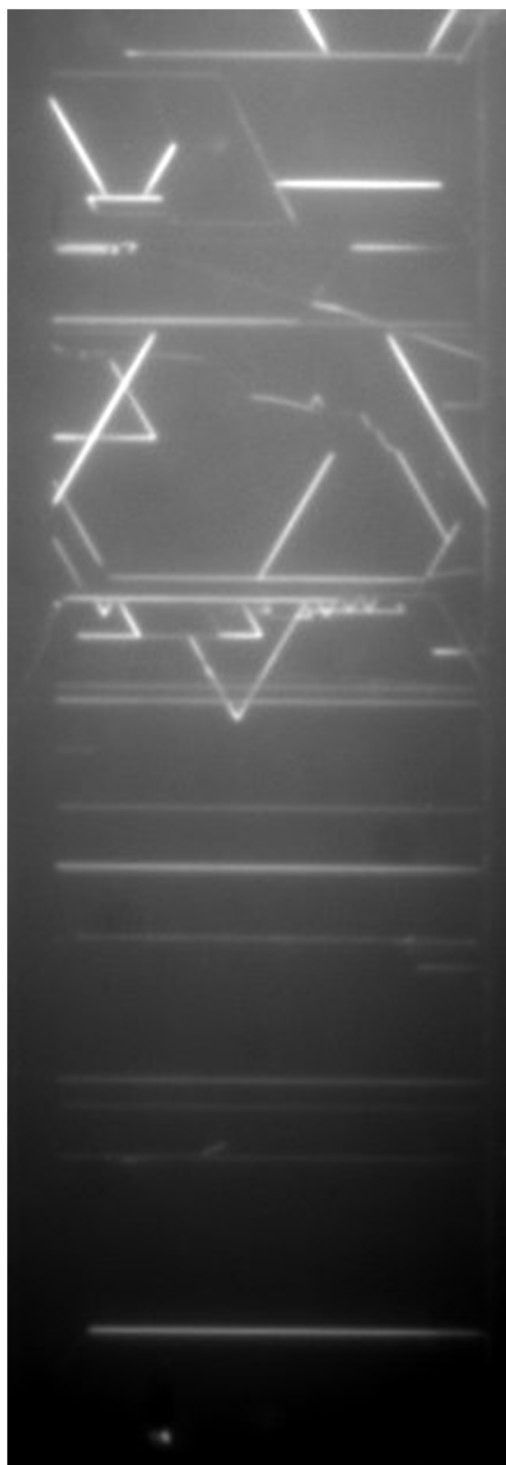

FIG. 3. Low magnification and high intensity in-situ UV-PL movie showing the evolution of dislocation glide over time using a LP > 700 nm filter. (Multimedia available online) Format.avi.
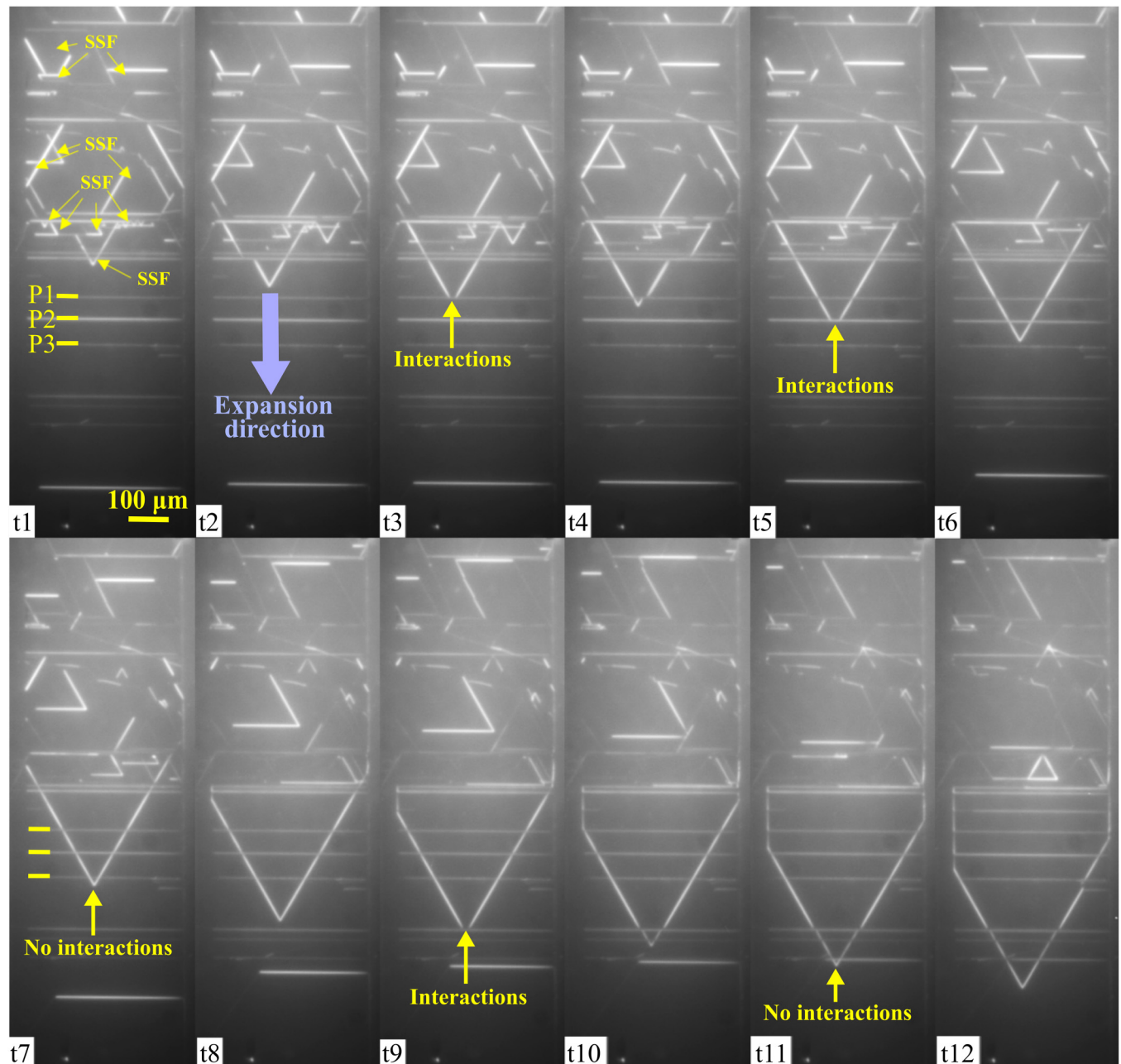
11 September 2023 21:39:17

FIG. 4. High intensity in-situ UV-PL images arbitrarily selected to best show the evolution of dislocation glide through time evolution t1-t12 using a LP > 700 nm filter.

Shockley SF expands downwards and interacts with P1 at t3 that is followed by a temporary pinning. The dislocations then hop through P1 and continue gliding at t4. The Shockley SF then expands and interacts with P2 at t5, but do not interact with P3 at t7. This means that this SF tracked is on the same basal plane as P1 and P2 but not on the same basal plane as P3. Therefore, these

trapezoidal defects have a certain volume associated to it in the epilayer as the SFs are spread over the length of the defect along the [1−100] direction. All of the Shockley SFs denoted at t1 originate in different locations within the trapezoidal defect tower at the fainter partials bounding the Frank-type SFs and expand on multiple different basal planes (different depths).
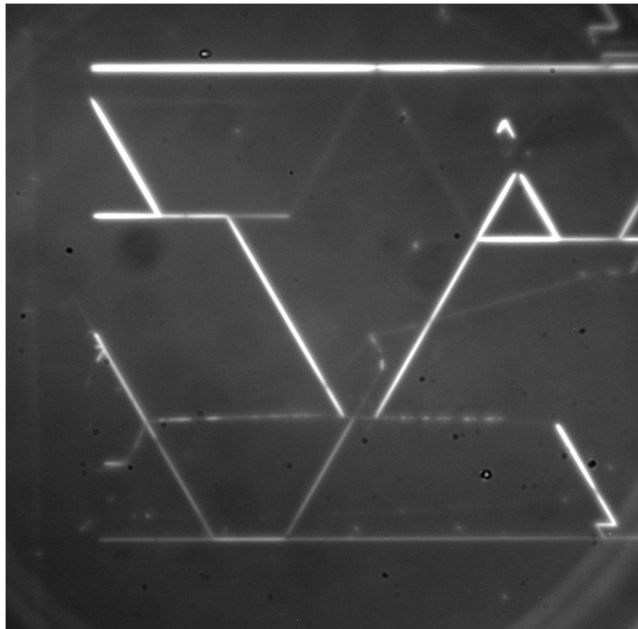
FIG. 5. High magnification and high intensity in-situ UV-PL movie showing the interaction between Si-core and C-core partials over time using a LP > 700 nm filter. (Multimedia available online). Format.avi.

The second *in situ* UVPL expansion imaging in Fig. 5 (Multimedia available online) is done at higher magnification in order to show closely how the evolution of glissile Si-core partials are bounded by sessile C-core partials. At time t1 in Fig. 6, the bright angled partials correspond to Si-core partials bounding SFs and are seen to expand at t2. In t3, we can clearly observe a triangular-shaped SF bounded by C-core partials with a dimmer emission. The C-core partials being on the same plane as the SSFs, interact with the bounded Si partials and prevent their expansion. The same phenomenon is observed at t6-t9 where the expansion of a SF is constrained by two [11–20] oriented partials (above and below the SF) limiting the expansion direction of the Si partials to only left and right as shown by the blue arrows in Fig. 6. At t6, as the SF expansion continues, the Si-partials bounding the SF are seen to adopt a zigzag configuration when encountering the bottom dislocation. According to Chen's work,[33] this zig-zag pattern is a metastable configuration that happens due to a change of dipole when a Si-partial expanding encounters a screw character TD before it snaps into screw orientation. Since trapezoidal defects are made of EFSFs bounded by dislocations with mixed character, this information is important as it confirms the screw character of these mixed dislocations. We can also notice that the [11–20] Si-partial at the top of UV-PL image at t1 goes through the C-core SF without interactions because they are on different basal planes. The glide of this dislocation is most noticeable from t1-t15. An interesting outcome from these UV-PL *in situ* experiments is that the expansion of Shockley SFs within the trapezoidal defects is highly limited due to temporary pinning [Fig. 4] or complete

constrainment between sessile dislocations [Fig. 6]. Next, CL is used to show the spectra associated to the different SFs observed in trapezoidal defects towers.

Microscale CLSI analysis was conducted on these defects from the two areas, in regions having the two luminescence signatures together or individually. Figures 7(a) and 7(b) show UV-PL images of areas 1 and 2 as well as the marked regions R1-R6 where the CLSI data were acquired. Figures 7(c)–7(h) show the global CL spectra with their corresponding peak photon energy maps from regions R1–R6. The peak photon energy map on region R1 shows the presence of the stacking fault emitting at ∼425 nm which corresponds to SF1 as expected from Table I identified earlier as either an extrinsic Frank-type SF or a single Shockley SF from the UV-PL images. From previous studies, it is safe to say that these stacking faults emitting in the UVPL images are Frank-type faults and therefore correspond to EFSFs. R3 shows the presence of a small region corresponding to an EFSF but the global spectra is dominated by a peak in emission near 450 nm corresponding to SF2. This stacking fault emitting at 450 nm has never been observed in trapezoidal towers before and their luminescence signal is a characteristic wavelength of multilayer Frank-type stacking faults or 8H-SF (Table I). The peak photon energy map for region R2 shows three regions with distinct emission spectra. The emission from subregion R2-II is due to the EFSF emitting at ∼430 nm as identified in the previous region. Subregion R2-III has a second peak at ∼450 nm and corresponds to SF2 while the last subregion R2-I is on the other side of the SF intersecting the surface and is where the near-band-edge (NBE) peak is observed. The same analysis was done on area 2 to confirm the emissions. Regions R4 show the two same luminescence signatures from EFSF and SF2 in subregions R4-II and R4-III, respectively. It has to be noted that R4 is near the middle (depth) in the epi and the luminescence we get from the stacking faults from right to left decreases accordingly (see Fig. S1 in the supplementary material for intensity profile). That is the reason why most of the left side of the peak photon energy map (R4-I) is shown to correspond to the NBE since it is only seeing photons from the defect free region as the stacking fault gets too deep on the basal plane. The luminescence peak gradually gets into shape when scanning along the step-flow direction from the substrate/epilayer interface to the surface substrate, due to the upstream formation of the fault on the basal plane. R5 shows the same emission for SF2 (R5-III) but a different emission than the EFSF in R5-II that is in the 425 nm range. Indeed, a really small triangular SF was observed in this region thus, the emission is due to the presence of a 1SSF in the region. This explains why the emission wavelength is shorter. R6 shows the presence of two EFSFs in R6-II. So far, the luminescence analysis revealed the presence of two types of SFs in the ∼ 420 nm range emission which are SSFs and EFSFs (identified as SF1 in the UV-PL imaging). For SF2, which gives out emission in the ∼450 nm range, it is still unclear whether it corresponds to an 8H-SF or a MFSF. The EBIC and TEM analysis provided below will help clarify the nature of this SF. To understand the recombination behavior of excess carriers at defect sites, SEM-EBIC was done on area 1 in a region having the two luminescence signatures defects [see Fig. 8].

The EBIC image in Fig. 8(a) shows that dislocations have the strongest EBIC contrasts, which confirms that BPDs are the most
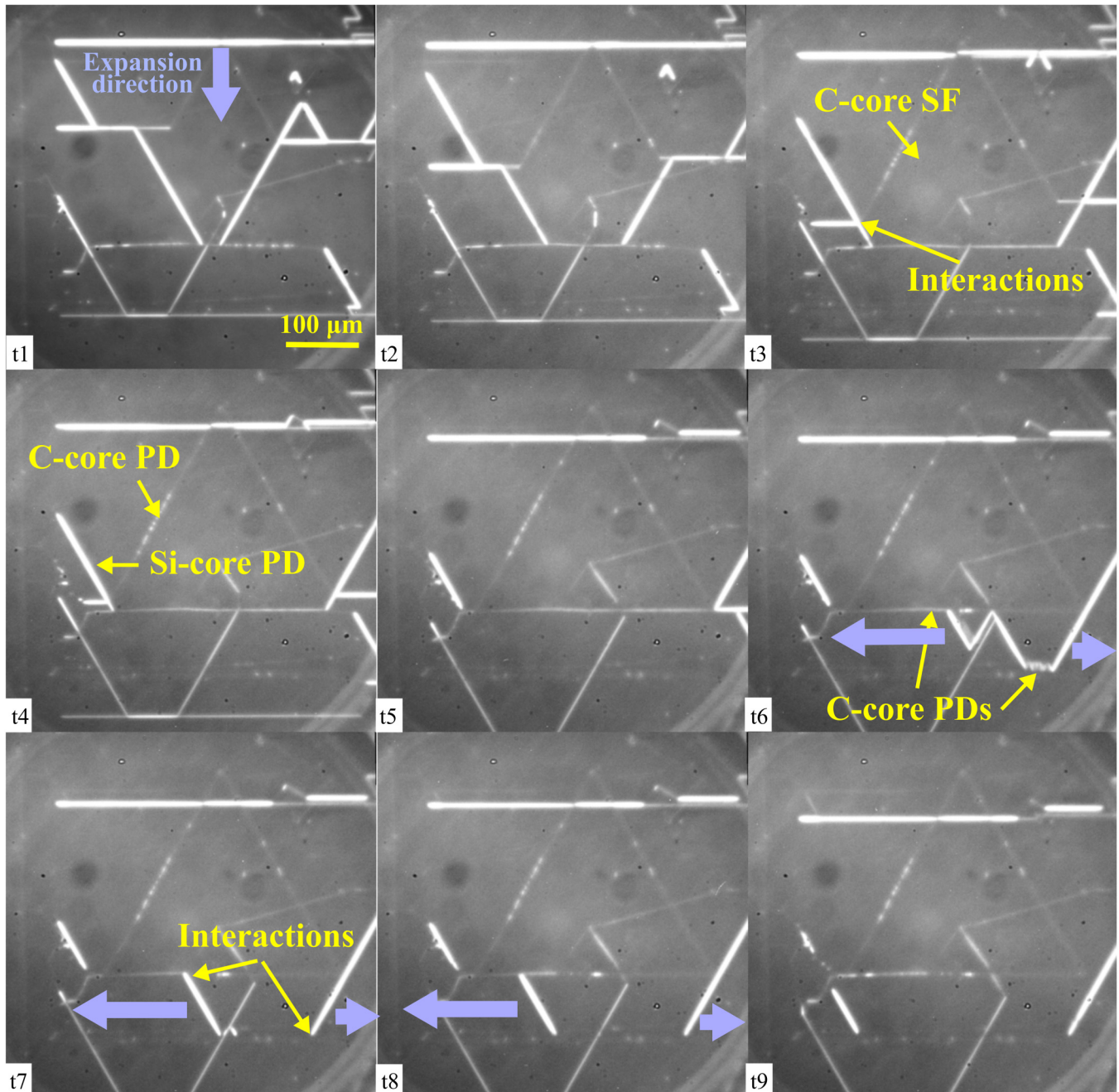
FIG. 6. High magnification and high intensity in-situ UV-PL images arbitrarily selected to best show the interaction between Si-core and C-core partials through time evolution t1–t9 using a LP > 700 nm filter.

electrically harmful in the 4H-SiC epitaxial films which is partially due to the geometry of the dislocations and higher density of recombination centers along the dislocation core. All the BPDs showing contrast in EBIC intersect the surface at the right end

since they are dislocation lines lying on the (0001) plane at 4° angle following the step-growth direction [11–20]. The core of Si- and C-partials are different and have different concentration of recombination centers due to their different chemical nature, which also
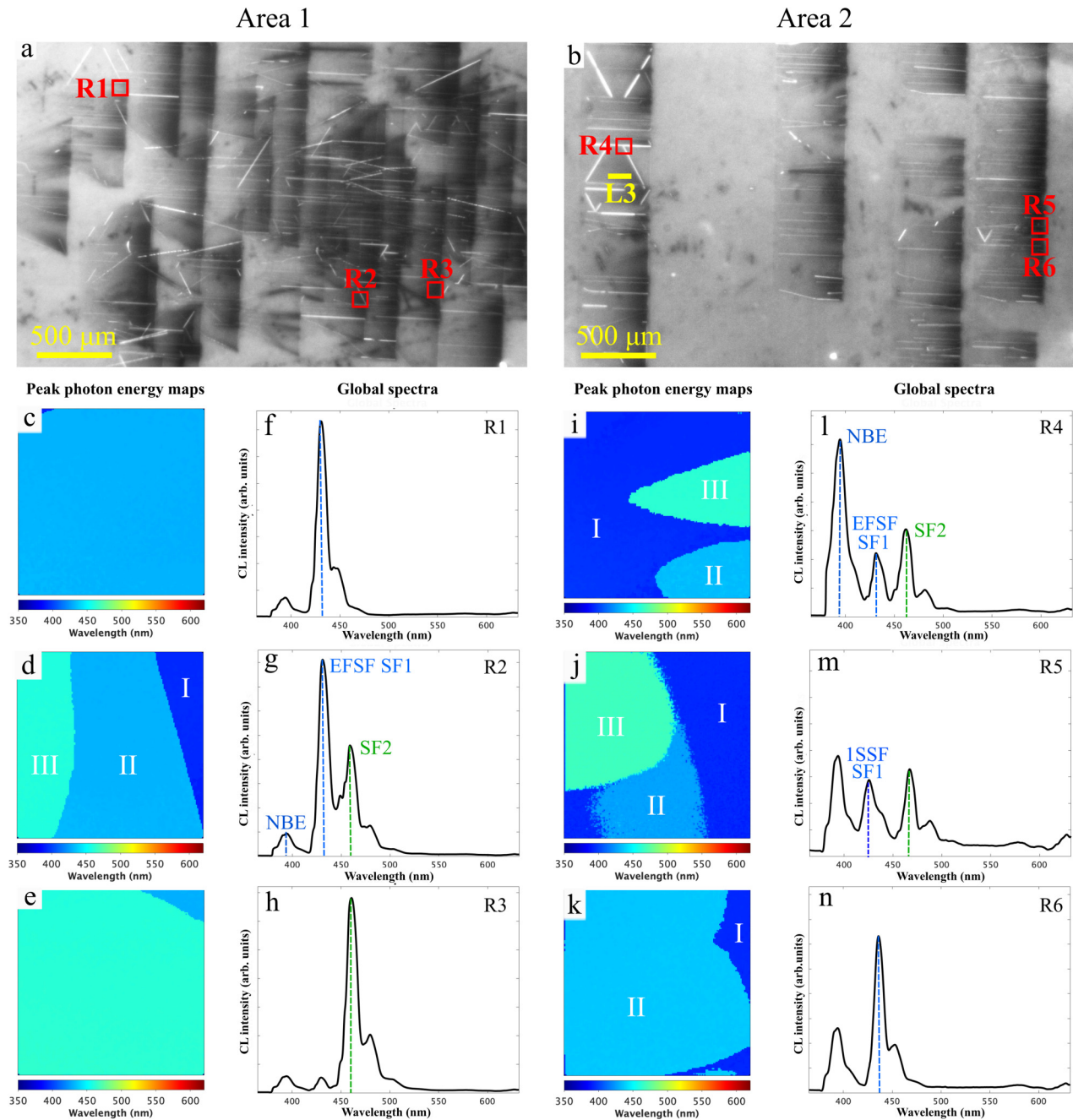
FIG. 7. UV-PL images LP > 700 nm of area 1 (a) and area 2 (b). CL peak photon energy maps (c–e), (i–k) and global CL spectra (f–h), (l–n) associated with regions R1-R6.
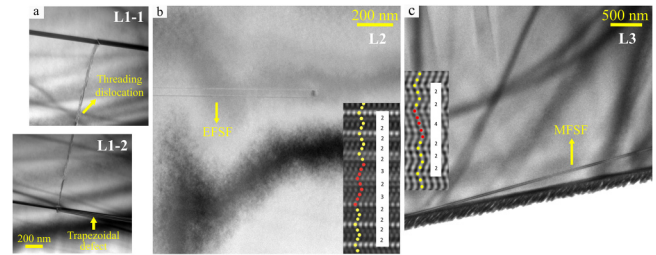
means that they should result in different EBIC contrasts.[2,4,16,17,19,33,34] However, no difference is observed as the difference is so small. Also, comparing their absolute EBIC contrast values is not accurate since they may vary with different specimen and sample preparation.

Other than dislocations, surface defects show strong dark contrast and are indicated in the figure. It should be pointed out that SFs delineated by the dark BPDs contrast are as bright as background, which is peculiar to SFs in SiC, since electrical active defects generally show dark contrast due to carrier recombination.
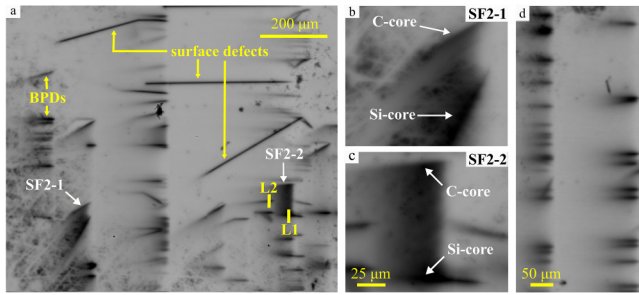
FIG. 8. (a) SEM-EBIC image at 15 kV on a region of area 1; (b) and (c) are cropped images from SFs emitting in the 450 nm range, labelled SF2-1 and SF2-2 in (a), respectively; (d) EBIC image at 15 kV showing more accurately the impact of the dislocations in the towers on carrier recombination. See Fig. S2 in the supplementary material and S3 for supplementary information.


FIG. 9. Bright field diffraction contrast TEM images of the bar-shaped stacking faults in lift-outs L1-L3. (a) L1 has two trapezoidal defects that are joined by a threading dislocation and taken under a diffraction condition g = {−1015}; (b) L2 has two trapezoidal defects joined by a threading dislocation taken under diffraction condition g = {−1015}; (c) L3 was lifted out from a SF emitting at 450 nm (see Fig. 7 for location) and shows a trapezoidal defect under diffraction condition g = {−1015}; The inset in images (b) and (c) are Fourier-filtered HR-TEM images looking down axis included in zone axis ⟨11–20⟩, showing the stacking sequence (2, 3, 2, 3) and (2, 4, 2), respectively, of the corresponding stacking faults observed.

Indeed, SFs emitting at 420 nm introduce a natural quantum-well state which is 0.25 eV lower than the conduction band edge of 4H-SiC. Camarda *et al.* have shown through Kohn–Sham band structures simulation along the closed path -M-K- in the Brillouin zone of the defect supercell that the EFSFs generate three intragap energy levels, responsible for the PL peak at 2.9 eV.[9] By this quantum-well state lowering, this EBIC signal can be explained. In EBIC, electron–hole pairs are generated in a pear-shaped volume via electron-beam irradiation at 15 kV. When the beam irradiates the material, the concentrations of generated electrons and holes in the volume add on to the intrinsic electron and hole concentrations at equilibrium already present in the material. At the SF, however, a considerable fraction of generated electrons is captured by the SF due to its lower quantum-well state as described above. Those electrons diffuse away along the SF, and consequently the electron density in the generation volume decreases. In EBIC, minority carriers generated by an electron beam are collected as the EBIC signals, i.e., holes in this work.[35,36] While electrons are captured by the quantum-well state, holes are not and diffuse freely in response to the electric field generated by the depletion regions. Thus, the lifetime of holes in the volume increases and as a result, the collected EBIC current at SF is as bright as that of the background. In contrary, it is observed that the stacking faults emitting at 450 nm have darker contrast in EBIC. The lifetime of holes around these stacking faults is shorter due to the deeper intragap state (∼2.65 eV) because electrons diffuse away along the stacking fault plane but the probability of recombination through this state is higher. It is to note that there is higher possibility of re-emission to the conduction band from an electron in the 2.9 eV state than in the 2.65 eV intragap state. Figures 8(b) and 8(c) show EBIC images at 15 kV of SF2-1 and SF2-2 that emit in the 450 nm range. Figure S2 in the supplementary material illustrates the glide of Si-core BPDs under electron-beam irradiation (RT) bounding these SFs. After a few minutes of electron-beam irradiation, SF2-1 and -2 were observed to have one stationary C-core partial and one leading Si-core partial expanding. The SF is clearly observed to become larger due to the continuous drag of the moving Si partial (refer to Fig. S2 in the supplementary material). The excess majority carriers generated by the e-beam induces the motion of the

already existing Shockley Si-partial by the REDG mechanism.[36,37] This is evidence of the Shockley nature of this stacking fault. Referring to Table I, this should correspond to the 8H-polytype. Thierry-Jebali *et al.*[20] also showed that 8H-SFs are commonly found around Frank-type SFs and Frank partials. In their report, they show the presence of triangular shaped SFs originating from Frank partials, in the exact same pattern as in Fig. 2, which they identify as 8H-SFs. Tsuchida *et al.*[38] made similar conclusions and they identified two different ways to create 8H-SF. The first one is the overlapping of Shockley faults (two double SFs) and the second is the overlapping of two Frank faults (intrinsic and extrinsic). While both are possible, the second way seems more likely to happen as trapezoidal defects are mostly composed of Frank-type stacking faults. Aoki *et al.*[39] found that trapezoidal defects can contain both intrinsic and extrinsic Frank-type SFs. The overlap of intrinsic and extrinsic SFs is therefore highly possible for the creation of 8H-SFs within trapezoidal defects.

Interestingly, one of the stacking faults also emitting at 450 nm did not expand under long exposure to the e-beam. This triangular stacking fault can be seen in Fig. 7(a) where lift-out L3 is located. L3 was lifted-out at the specific location indicated by the yellow bar on the UV-PL image. The TEM results below will discuss the nature of this fault.

In order to investigate the crystallographic structure of the defects previously identified, a HR-TEM analysis was done. The samples were prepared to perform a cross-sectional analysis of the stacking faults and were oriented in order to intercept defects coming toward the surface or along the step growth direction from the trapezoidal defects. They are indicated as L1–L3 and are marked in Figs. 5 and 6. Bright field, diffraction contrast, and cross-sectional TEM images of the bar-shaped stacking faults from L1–L3 are shown in Figs. 9(a)–9(c) respectively. These were all acquired after tilting approximately 20° from the ⟨10 − 10⟩ pole and using a g = {−1105} two beam diffraction condition. The TEM images clearly reveal the presence of stacking faults on the basal plane. The HR-TEM inset images for L2 and L3 in Figs. 9(b) and 9(c) are
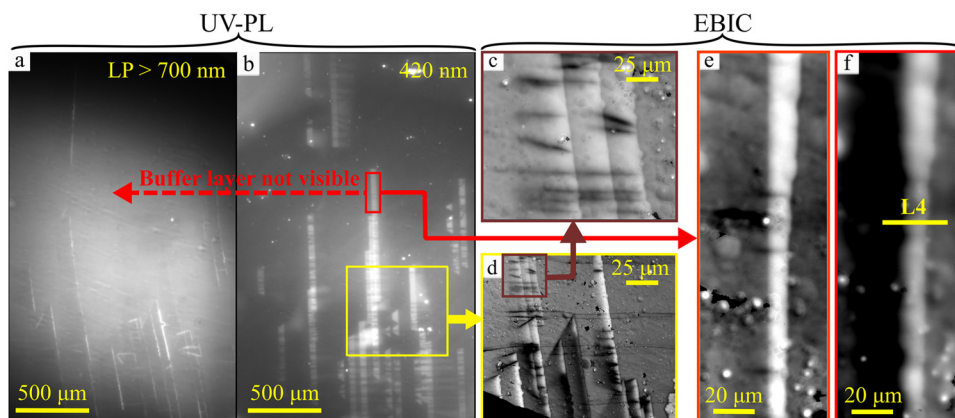
FIG. 10. (a) UV-PL image LP > 700 nm and (b) bandpass 420 nm of area 1 after 29.7 um were removed via low-angle milling in the center of the area; (c–f) EBIC images. See Fig. S4 in the supplementary material for supplementary information.

Fourier filtered HR-TEM images acquired looking along the $\langle 10-20 \rangle$ zone axis. These images allowed for the determination of the defect's stacking sequence discussed below. As indicated Fig. 8, L1 was lifted-out along [1–100] in a region where trapezoidal defects overlapped. An important observation from L1-1 and L1-2 in Fig. 9(a) is that two trapezoidal defects are joined by, likely, a threading screw dislocation (TSD). This observation was made in a few other samples where trapezoidal defects overlapped. As shown in Chen's work, when an advancing Shockley partial dislocation encounters a TSD, a prismatic stacking fault is nucleated and has sessile configuration.[33] Thus, in this type of overlapped regions, the accumulation of defects, such as TSDs, can be more detrimental to device performance leading to a local increase in recombination sites.

L2 was lifted out from a stacking fault emitting at 420 nm along the [1–100] direction while L3 was lifted out from a SF emitting at 450 nm and along [11–20] due to the depth of stacking fault. The Fourier filtered HR-TEM image in Fig. 9(b) confirms previous reports that these towers are mainly composed of extrinsic Frank-type SFs with a (. . .2, 3, 2, 3, 2. . .) stacking sequence in the Zhdanov's notation.[8,9] It is important to note that the intensity of the PL emission and wavelength shift could vary with the width of the faulted region because more electron–hole pairs accumulate and recombine in a thicker faulted region. A more compact notation for this SF is $(2,3)_n$, with n indicating the number of (…2, 3…) layers. The inset Fourier filtered HR-TEM image of the newly discovered stacking fault in L3 shows that its stacking sequence is (…2, 4, 2…). Referring to Table I, this SF corresponds to a multi-layer Frank-type SF. Therefore, we have evidence that EFSF, SSF, 8H-SF and MFSF are present in trapezoidal defects.

In order to investigate the origin of trapezoidal defects, low-angle Argon ion milling was performed on top of area 1 (see Fig. S4 in the supplementary material). The sample was rotated during milling, and a concave shape crater was formed where the deepest area (the center) had 29.750 μm out of the 30 μm of the epilayer thickness removed. Figure 10(a) shows a UV-PL image of this area acquired with a long-pass filter >700 nm to observe the dislocation network after milling. However, since we are now located in the buffer layer in the center and close to the substrate, the stacking faults and dislocations are hardly visible due to high background doping concentration. The gradient of thickness can also be noticed by seeing the stacking fault projected width increasing from the center of the image to the corners reflecting the concave shape crater. In order to locate accurately the SF in the buffer layer, the 420 nm filter was used to obtain luminescence only from the trapezoidal defects [Fig. 10(b)]. EBIC was then performed on the red, brown, and yellow boxed regions highlighted in Figs. 10(c)–10(f). In order to check for the presence of the SF in the substrate, the accelerating voltage was increased to 30 kV [Fig. 10(f)] due to high doping level in the substrate. The dark band contrast appearing on the left of the bright EBIC signal means that the SF is from the substrate and propagates into the epilayer. We noticed that the SFs appear much brighter than EBIC
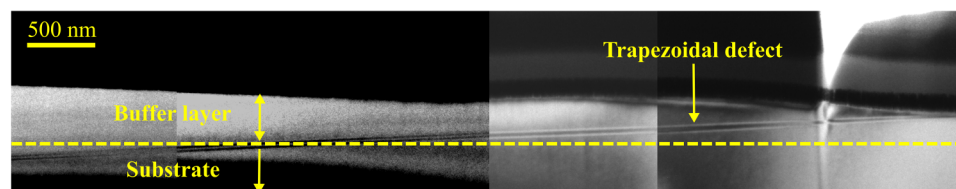
FIG. 11. Bright field two beam condition diffraction contrast TEM images of a trapezoidal defect lifted out after low-angle milling (see Fig. 10 for location) taken under diffraction condition g = {−1105}. The trapezoidal defect is shown to originate from the substrate and propagate through the buffer layer to the epi. No contrast difference was observed between substrate, buffer layer and epilayer.

measurements before milling. This is still unclear as it could come from various external sources during experiments or due to intrinsic properties when performing EBIC closer to the interface substrate/epilayer. Lift-out L4 was made to confirm the existence of the SF in the substrate. Figure 11 shows bright-field {−1105} two beam condition diffraction contrast TEM images, obtained after tilting the sample approximately 20 degrees from the ⟨10 − 10⟩ pole,

stitched together to best show the SF propagation from the substrate to buffer layer. The yellow dashed line roughly indicates the boundary between the 4H-SiC buffer-layer and the substrate region.

The fact that these bar-shaped stacking faults already exist in the substrates and are replicated in the epitaxial layers means that the density of bar-shaped stacking faults found in an epilayer
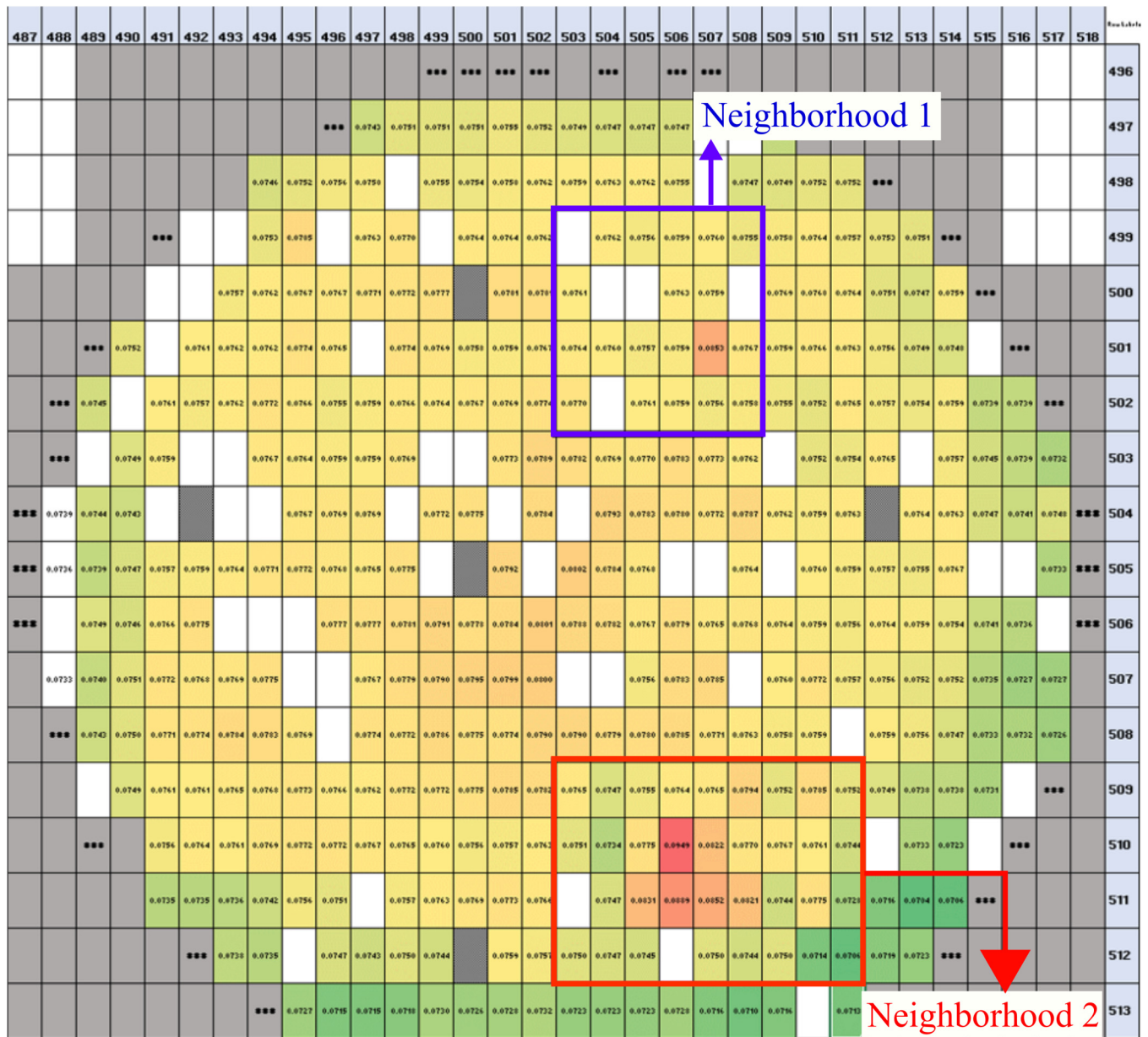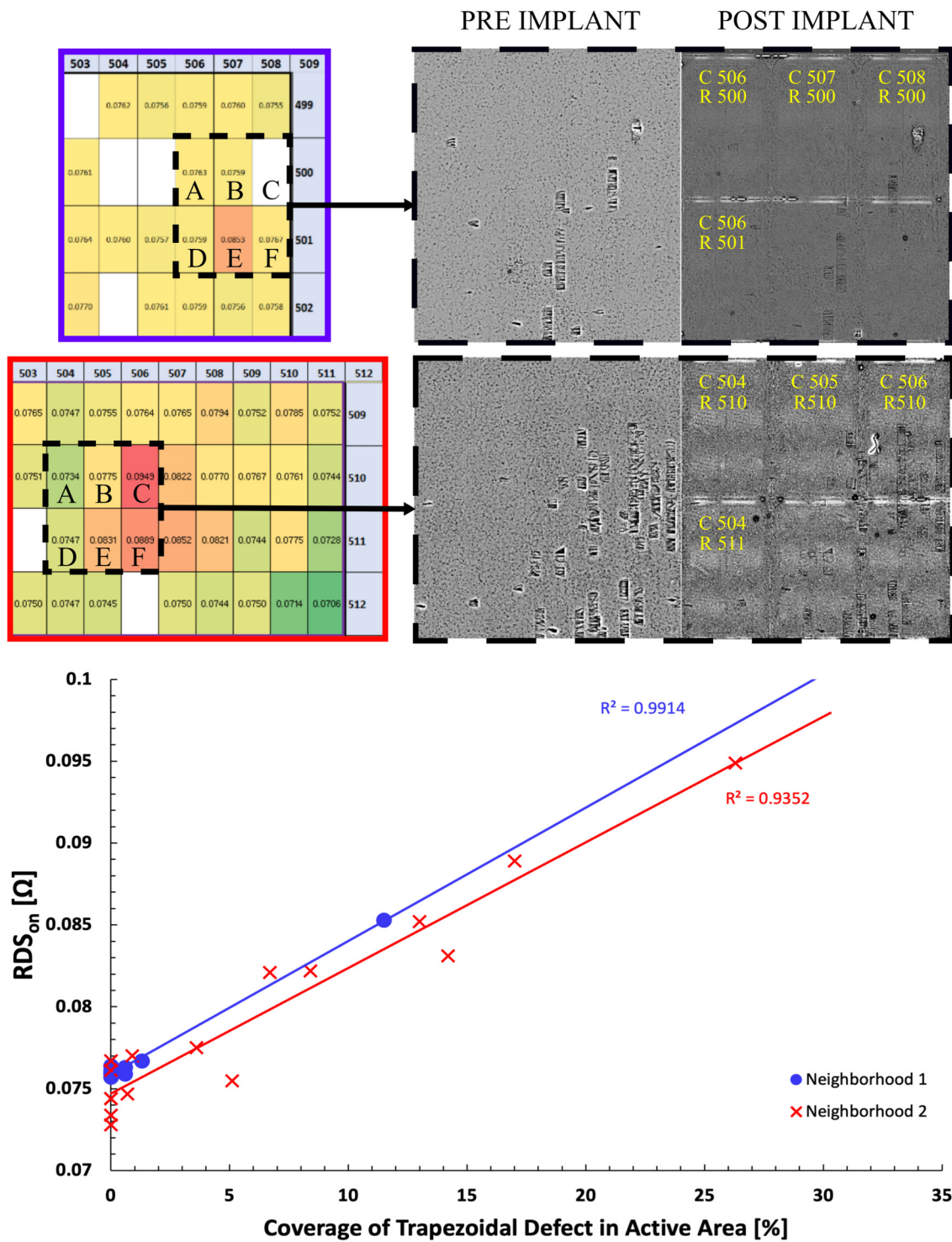

FIG. 12. On-state resistance map of a processed wafer showing the localized effect of trapezoidal defects on MOSFETs RDS$_{on}$ in neighborhoods 1 and 2. The die size is 7 mm by 4.5 mm.

FIG. 13. RDS$_{on}$ variation with percentage coverage of trapezoidal defect in the epilayer for each MOSFET in neighborhoods 1 and 2. The data used for the plot are showed in Tables SI and SII (in supplemental information). The linear fit shows that an increase in % coverage of trapezoidal defects in both neighborhoods leads to an increase in RDS$_{on}$. UV-PL images pre- and post-implant show the area covered by trapezoidal defects in each die.

strongly depends on the substrates employed for epitaxial growth. Up till now, the origin of this defect is unclear. However, the results provided in this paper could lead to a better understanding of their origin. These lines are oriented in the [1–100] direction and correspond to an array of dislocations following the a-plane in the 4H-SiC HCP crystal system. From the surface defects observed in the EBIC images in Fig. 8(a) and the occurrence of multiple array of dislocations in the same region, it is safe to say that these defects occur in highly strained boule growth. This study also revealed the screw type character of partials that bound the EFSF in these towers. These partials have a c-component to the burgers vector which also means, by the invariance or conservation of the total Burgers vector, the threading dislocation array was made of threading mixed dislocations (TMDs) or TSDs (if pure screw type). The dissociation into partial dislocations (from TMDs or TSDs) restricts screw motion to the plane of the stacking fault. Cross slip requires that the partial dislocations re-associate, cross slip as a unit dislocation, and then re-dissociate on the new slip plane. These partials do not move thus, do not constrict and so do not convert. Different groups reported that basal plane dislocations that propagate into the epilayer (originate from the substrate) have their Burgers vector along the off-cut direction, i.e., all of them are screw type.[37,40–42] This is consistent with our observation where these partial dislocations do not convert and perfectly replicate while going through the substrate/buffer layer and buffer layer/epilayer interface. The screw character of the threading dislocation array would also explain the presence of SFs on multiple basal planes. From these observations, one can tell that such arrays are generated in regions with major type of deformations such as high lattice tilts, dilatation or compression which could be occurring during the boule growth or seed crystal formation.

Figure 12 shows the on-state resistance map of MOSFETs as-fabricated on the wafer with a die size of 7 mm by 4.5 mm. It should be noted that slight process-induced variations in RDS$_{on}$ is typically seen across a given wafer, which can be attributed to minor wafer doping and process variations. Therefore, when looking at RDS$_{on}$ variation for the purpose of correlating to trapezoidal defects, it was decided to focus on neighborhoods of devices on the wafer. In the data presented, two neighborhoods having trapezoidal defects are circled. The green color corresponds to low RDSon values while the red color corresponds to the highest RDSon values (white colored die are failed devices). It can be observed that the two neighborhoods having trapezoidal defects have a local increase in RDSon values. Out of a 12 wafers lot, half of the wafers contained trapezoidal defects. The effect of trapezoidal defects on RDS$_{on}$ was repeatedly observed across these wafers.

Figure 13 provides a detailed analysis of the impact of these defects on MOSFETs RDS$_{on}$. Tables SI and SII present the coordinates of the die with corresponding RDS$_{on}$ and percentage covered by trapezoidal defects in the active area of the die. In Fig. 13, the RDSon values of each die in the respective neighborhoods are presented with their UV-PL images for adequate correlations. In the two neighborhoods, plotting RDS$_{on}$ vs % active area with trapezoidal defect clearly suggests that these defects lead to an increase in the RDS$_{on}$ as the % coverage increases. This effect on RDS$_{on}$ is believed to simply be due to the defective crystal structure disrupting electron flow through the vertical MOSFET therefore adding

another resistance component to the RDS$_{on}$ series resistance. While the low percentage values seem to not have a drastic impact on device performance, die (506, 510) and die (506, 511) with 26.30% and 17% covered active area, respectively, have failed due to high reduction in breakdown voltage (BVDSS failure). These two respective devices had the highest RDS$_{on}$ values with 0.0949 and 0.0889. As a reminder, an increase in RDS$_{on}$ means lower current rating for MOSFETs devices and higher power loss. Based on this result, we speculate that there is a threshold value = % area covered by trapezoidal defects that brings the device to failure. From these observations, it is safe to assume that devices with trapezoidal defects have higher leakage than defect-free devices as it is commonly known to happen in devices having SFs. In general, the SFs act as recombination centers and introduce electronic states in the middle of the bandgap which, in turn, behave as generation centers when the body diode is biased, causing a higher leakage current. At defect locations, the carrier lifetime is poor and lower carrier lifetime leads to a larger resistance. Since this defect intersects the surface as shown in EBIC [Fig. 8], the majority carrier conduction in the drift layer will be directly affected since electron trapping would severely limit the flow of electrons. This could lead to high leakage in the channels and cause low mobility. This defect will consequently affect the behavior of first and third quadrant operations in MOSFETs. It is to note that the percentage covered by the defect in the active area is calculated only using the area seen in the UV-PL images and therefore only accounts for the area covered by the defects in the drift layer since it is the most harmful to device performance. The trapezoidal defect impact on RDS$_{on}$ will be the area percentage of this defect relative to the active transistor area.

IV. SUMMARY

This study uses a multi-scale luminescence characterization approach coupled to a structural and electrical analysis to provide a detailed understanding of the optoelectronic properties and atomic structure of trapezoidal defects in SiC, and their adverse impact on the performance of 4H-SiC MOSFETs. To begin with, the bar-shaped stacking faults were identified by the PL and CL measurements to be made of SFs with peak emission wavelengths of ~420 nm and ~450 nm. The correlation between the luminescence and microscopy results allowed us to precisely identify the nature of all the SFs present in these towers which are: SSFs, EFSFs $(2,3)_n$, MFSF (4, 2), and 8H-SF. Then, the optoelectronic behavioral study done at different magnification showed that: Shockley SF (most likely 8H-SFs) originate at C-core partials; trapezoidal defects are spread on multiple basal planes; SFs do not extend over the basal plane they are in; the expansion of some of the SFs is constrained by sessile partials on the same basal plane (which in part can be beneficial to body diode degradation) while other SFs are temporally pinned before continuing the expansion. EBIC imaging showed that the high density of dislocations in these towers act as strong sites of carrier recombination which is likely to have an impact on the on-state transfer characteristics of SiC devices. It was found that the 420 nm emitting SFs EBIC signal was as bright as background while stacking faults emitting in the 450 nm range showed stronger EBIC contrast. The TEM analysis showed that threading dislocations are often found joining trapezoidal defects at

different depth which can result in the formation of sessile prismatic faults. EBIC and TEM also revealed that trapezoidal defects come from the substrate and propagate into the epilayer. Furthermore, device electrical measurements have shown that this type of defect impacts the electrical performance of MOSFETs via an increase in the on-state resistance. More specifically, our research has uncovered that as the percentage coverage of trapezoidal defects increases within the active area of a MOSFET device, the RDSon increases. Overall, our conclusions find that trapezoidal defects should still be considered non-killer (at low % coverage), but efforts by substrate and epi manufactures need to be made to continue to reduce the incidence of trapezoidal defects. The correlation between the set of data provided allowed for the complete understanding of this defect which is necessary to help prevent its occurrence. Further study should be made to understand any other electrical effects that trapezoidal defects may cause in SiC MOSFETs.

SUPPLEMENTARY MATERIAL

See the supplementary material S1 for the support of Fig. 7 and is an intensity profile proving that the luminescence signal from the stacking faults from right to left decreases. Figure S2 is in support of Fig. 8 and shows the behavior of Si and C-core dislocations under e-beam irradiation. Figure S3 is also in support of Fig. 8 and shows the photoluminescence images of the same area where EBIC was performed. Figure S4 supports Fig. 10 and shows the UV-PL images on the same area before and after low-angle ion milling was done for better visualization. Tables SI and SII show the raw data used in support of the graph in Fig. 13. Two video files were uploaded in order to support the UV-PL *in situ* experiments in Figs. 4 and 6 by showing the behavior of dislocations in real time.

ACKNOWLEDGMENTS

AUTHOR DECLARATIONS

Conflict of Interest

The authors have no conflicts to disclose.

Author Contributions

Sami A. El Hageali: Conceptualization (equal); Formal analysis (equal); Investigation (equal); Methodology (equal); Writing – original draft (equal); Writing – review & editing (lead). **Harvey Guthrey:** Conceptualization (equal); Methodology (equal); Writing – review & editing (equal). **Steven Johnston:** Conceptualization (equal); Methodology (equal); Writing – review & editing (equal). **Andrew Norman:** Methodology (equal); Writing – review & editing (equal). **Jake Soto:** Resources (equal); Writing – review & editing (equal). **Bruce Odekirk:** Resources (equal); Writing – review & editing (equal). **Robert E. Stahlbush:** Conceptualization (equal); Writing – review & editing (equal). **Nadeemullah A. Mahadik:** Conceptualization (equal); Writing – review & editing (equal). **Brian P. Gorman:** Supervision (equal); Writing – review & editing (equal). **Mowafak Al-Jassim:** Supervision (equal); Writing – review & editing (equal).

DATA AVAILABILITY

The data that support the findings of this study are available from the corresponding author upon reasonable request.

REFERENCES

[1]I. R. L. Myers-ward, V. A. Us, D. K. Gaskill, and C. R. Eddy, U.S. patent (Oct. 11, 2016).

[2]A. Galeckas, J. Linnros, and P. Pirouz, "Recombination-enhanced extension of stacking faults in 4H-SiC p-i-n diodes under forward bias," Appl. Phys. Lett. **81**(5), 883–885 (2002).

[3]J. D. Caldwell, R. E. Stahlbush, M. G. Ancona, O. J. Glembocki, and K. D. Hobart, "On the driving force for recombination-induced stacking fault motion in 4H-SiC," J. Appl. Phys. **108**(4), 044503 (2010).

[4]M. Skowronski, J. Q. Liu, W. M. Vetter, M. Dudley, C. Hallin, and H. Lendenmann, "Recombination-enhanced defect motion in forward-biased 4H-SiC p-n diodes," J. Appl. Phys. **92**(8), 4699–4704 (2002).

[5]K. Maeda, K. Suzuki, and M. Ichihara, "Recombination enhanced dislocation glide in silicon carbide observed *in-situ* by transmission electron microscopy," Microsc. Microanal. Microstruct. **4**(2–3), 211–220 (1993).

[6]S. A. El Hageali, H. Guthrey, S. Johnston, J. Soto, B. Odekirk, B. P. Gorman, and M. Al-Jassim, "Nondestructive microstructural investigation of defects in 4H-SiC epilayers using a multiscale luminescence analysis approach," J. Appl. Phys. **131**(18), 185705 (2022).

[7]R. Stahlbush, N. Mahadik, P. Bonanno, J. Soto, B. Odekirk, W. Sung, and A. Agarwal, "Defects in 4H-SiC epilayers affecting device yield and reliability," IEEE Int. Reliab. Phys. Symp. Proc. **2022**, P651–P656 (2022).

[8]M. Aoki, H. Kawanowa, G. Feng, and T. Kimoto, "Characterization of bar-shaped stacking faults in 4H-SiC epitaxial layers by high-resolution transmission electron microscopy," Jpn. J. Appl. Phys. **52**(6 Pt 1), 061301 (2013).

[9]M. Camarda, A. Canino, A. La Magna, F. La Via, G. Feng, T. Kimoto, M. Aoki, and H. Kawanowa, "Structural and electronic characterization of (2, 33) bar-shaped stacking fault in 4H-SiC epitaxial layers," Appl. Phys. Lett. **98**(5), 051915 (2011).

[10]R. A. Berechman, S. Chung, G. Chung, E. Sanchez, N. A. Mahadik, R. E. Stahlbush, and M. Skowronski, "Trapezoid defect in 4HSiC epilayers," J. Cryst. Growth **338**(1), 16–19 (2012).

[11]L. Lilja, J. U. Hassan, E. Janzén, and J. P. Bergman, "In-grown stacking-faults in 4H-SiC epilayers grown on 2° off-cut substrates," Phys. Status Solidi Basic Res. **252**(6), 1319–1324 (2015).

[12]J. D. Caldwell, R. E. Stahlbush, and N. A. Mahadik, "Mitigating defects within silicon carbide epitaxy," J. Electrochem. Soc. **159**(3), R46–R51 (2012).

[13]D. Baierhofer, "Current SiC power device development, material defect measurements and characterization at bosch," Eur. Solid-State Device Res. Conf. **2019**, 31–34 (2019).

11 September 2023 21:39:17

[14] M. Nagano, I. Kamata, and H. Tsuchida, "Photoluminescence imaging and discrimination of threading dislocations in 4H-SiC epilayers," Mater. Sci. Forum **778–780**, 313–318 (2014).

[15] C. Kawahara, J. Suda, and T. Kimoto, "Identification of dislocations in 4H-SiC epitaxial layers and substrates using photoluminescence imaging," Jpn. J. Appl. Phys. **53**(2 Pt 1), 020304 (2014).

[16] K. X. Liu, X. Zhang, R. E. Stahlbush, M. Skowronski, and J. D. Caldwell, "Differences in emission spectra of dislocations in 4H-SiC epitaxial layers," Mater. Sci. Forum **600–603**, 345–348 (2008).

[17] K. X. Liu, R. E. Stahlbush, S. I. Maximenko, and J. D. Caldwell, "Differences in emission spectra of Si- and C-core partial dislocations," Appl. Phys. Lett. **90**(15), 153503 (2007).

[18] J. Nishio, A. Okada, C. Ota, and M. Kushibe, "Photoluminescence analysis of individual partial dislocations in 4h-SiC epilayers," Mater. Sci. Forum **1004**, 376–386 (2020).

[19] S. Ha, M. Benamara, M. Skowronski, and H. Lendenmann, "Core structure and properties of partial dislocations in silicon carbide p-i-n diodes," Appl. Phys. Lett. **83**(24), 4957–4959 (2003).

[20] N. Thierry-Jebali, C. Kawahara, T. Miyazawa, H. Tsuchida, and T. Kimoto, "Application of UV photoluminescence imaging spectroscopy for stacking faults identification on thick, lightly n-type doped, 4°-off 4H-SiC epilayers," AIP Adv. **5**(3), 037121 (2015).

[21] G. Feng, J. Suda, and T. Kimoto, "Characterization of stacking faults in 4H-SiC epilayers by roomerature microphotoluminescence mapping," Appl. Phys. Lett. **92**(22), 221906 (2008).

[22] G. Feng, J. Suda, and T. Kimoto, "Triple Shockley type stacking faults in 4H-SiC epilayers," Appl. Phys. Lett. **94**(9), 091910 (2009).

[23] S. Izumi, H. Tsuchida, I. Kamata, and T. Tawara, "Structural analysis and reduction of in-grown stacking faults in 4H-SiC epilayers," Appl. Phys. Lett. **86**(20), 1–3 (2005).

[24] M. Marinova, T. Robert, S. Juillaguet, I. Tsiaoussis, N. Frangis, E. Polychroniadis, J. Camassel, and T. Chassagne, "Combined structural and optical studies of stacking faults in 4H-SiC layers grown by chemical vapour deposition," Phys. Status Solidi Appl. Mater. Sci. **206**(8), 1924–1930 (2009).

[25] I. Kamata, X. Zhang, and H. Tsuchida, "Photoluminescence of Frank-type defects on the basal plane in 4H-SiC epilayers," Appl. Phys. Lett. **97**(17), 1–4 (2010).

[26] S. G. Sridhara, T. J. Eperjesi, R. P. Devaty, and W. J. Choyke, "Penetration depths in the ultraviolet for 4H, 6H and 3C silicon carbide at seven common laser pumping wavelengths," Mater. Sci. Eng. B **61–62**, 229–233 (1999).

[27] Y. Z. Yao, Y. Sugawara, Y. Ishikawa, H. Saitoh, K. Danno, H. Suzuki, Y. Kawai, and N. Shibata, "A simultaneous observation of dislocations in 4H-SiC epilayer and n +-substrate by using electron beam induced current," J. Appl. Phys. **109**(12), 123524 (2011).

[28] T. A. G. Eberlein, R. Jones, and A. T. Blumenau, "Theory of dislocations in SiC: The effect of charge on kink migration," Mater. Sci. Forum **527–529**, 321–326 (2006).

[29] R. Hirano, Y. Sato, H. Tsuchida, M. Tajima, K. M. Itoh, and K. Maeda, "Photoluminescence study of radiation-enhanced dislocation glide in 4H-SiC," Appl. Phys. Express **5**(9), 091302 (2012).

[30] M. Zhang, P. Pirouz, and H. Lendenmann, "Transmission electron microscopy investigation of dislocations in forward-biased 4H-SiC p-i-n diodes," Appl. Phys. Lett. **83**(16), 3320–3322 (2003).

[31] A. O. Konstantinov and H. Bleichner, "Bright-line defect formation in silicon carbide injection diodes," Appl. Phys. Lett. **71**(25), 3700–3702 (1997).

[32] G. Savini, M. I. Heggie, S. Öberg, and P. R. Briddon, "Electrical activity and migration of 90° partial dislocations in SiC," New J. Phys. **9**(1), 6 (2007).

[33] Y. Chen, *Defects Structures in Silicon Carbide Bulk Crystals, Epilayers and Devices* (State University of New York at Stony Brook, 2008).

[34] K. X. Liu, R. E. Stahlbush, M. E. Twigg, J. D. Caldwell, E. R. Glaser, K. D. Hobart, and F. J. Kub, J. Electron. Mater. **36**, 297–306 (2007).

[35] E. B. Yakimov, G. Regula, and B. Pichaud, "Cathodoluminescence and electron beam induced current investigations of stacking faults mechanically introduced in 4H-SiC in the brittle domain," J. Appl. Phys. **114**(8), 1–5 (2013).

[36] B. Chen, J. Chen, T. Sekiguchi, T. Ohyanagi, H. Matsuhata, A. Kinoshita, H. Okumura, and F. Fabbri, "Electron-beam-induced current study of stacking faults and partial dislocations in 4H-SiC Schottky diode," Appl. Phys. Lett. **93**(3), 29–31 (2008).

[37] H. Jacobson, J. Birch, R. Yakimova, M. Syväjärvi, J. P. Bergman, A. Ellison, T. Tuomi, and E. Janzén, "Dislocation evolution in 4H-SiC epitaxial layers," J. Appl. Phys. **91**(10 I), 6354–6360 (2002).

[38] H. Tsuchida, I. Kamata, and M. Nagano, "Investigation of defect formation in 4H-SiC epitaxial growth by x-ray topography and defect selective etching," J. Cryst. Growth **306**(2), 254–261 (2007).

[39] M. Aoki, H. Kawanowa, G. Feng, and T. Kimoto, "Characterization of bar-shaped stacking faults in 4H-SiC epitaxial layers by high-resolution transmission electron microscopy," Jpn. J. Appl. Phys. **52**(6 Pt 1), 1–5 (2013).

[40] H. Tsuchida, M. Ito, I. Kamata, and M. Nagano, "Fast epitaxial growth of 4H-SiC and analysis of defect transfer," Mater. Sci. Forum **615–617**, 67–72 (2009).

[41] T. Ohno, H. Yamaguchi, S. Kuroda, K. Kojima, T. Suzuki, and K. Arai, "Influence of growth conditions on basal plane dislocation in 4H-SiC epitaxial layer," J. Cryst. Growth **271**(1–2), 1–7 (2004).

[42] T. Ohno, H. Yamaguchi, S. Kuroda, K. Kojima, T. Suzuki, and K. Arai, "Direct observation of dislocations propagated from 4H-SiC substrate to epitaxial layer by x-ray topography," J. Cryst. Growth **260**(1–2), 209–216 (2004).

11 September 2023 21:39:17